International Journal of Heat and Mass Transfer 177 (2021) 121515

Contents lists available at ScienceDirect

International Journal of Heat and Mass Transfer

journal homepage: www.elsevier.com/locate/hmt

Unsteady RANS simulation of fluid dynamic and heat transfer in an oblique self-oscillating fluidic oscillator array

Tingzhen Ming[a,b], Zhiyi Wang[a], Xiwang Liao[a], Tianhao Shi[a], Gangfeng Tan[c], Yongjia Wu[a,*]

[a] School of Civil Engineering and Architecture, Wuhan University of Technology, Wuhan 430070, China
[b] School of Architecture Engineering, Huanggang Normal University, Huanggang 438000, China
[c] School of Automotive Engineering, Wuhan University of Technology, Wuhan 430070, China

ARTICLE INFO

Article history:
Received 2 January 2021
Revised 15 April 2021
Accepted 17 May 2021
Available online 5 June 2021

Keywords:
Fluidic oscillator
Heat transfer enhancement
Impinging jet
Numerical simulation

ABSTRACT

Impinging jet played an important role in cooling technology. The steady-state jet could be transformed into an oscillatory one based on the intrinsic flow instability mechanisms by using self-oscillating fluidic oscillators. In this paper, a high-performance microchannel heat exchanger based on a fluidic oscillator array was presented. The fluidic oscillators were tilted at an angle of 30° above the impinging surface to extend the influence area of the jets. The unsteady RANS turbulence models were adopted to study the fluid dynamic and heat transfer performance of the jet array. The time-resolved pressure field and velocity field were calculated to show that the parallel oscillators would produce three modes, including co-directional oscillation, reverse oscillation, and irregular oscillation, under synchronous and asynchronous output phases. The sweeping jets improved the heat removal performance by increasing the average Nusselt number and enlarging the influence range on the external flow field. The heat removal performance of the sweeping jets was almost equivalent under different oscillation modes.

1. Introduction

With the rapid increase of the heat fluxes released from microelectronic devices, thermal management technology faced great challenges [1]. The conventional heat sinks, pin fin arrays, fan-assisted heat sinks cooled by air had almost reached their limit of approximately 100W/cm^2 [2]. Impinging jet technology was usually used in the industrial production of cooling, heating, and drying. It could effectively destroy the boundary layer, increase disturbance inside the fluid, and enhance heat transfer capacity [3]. However, as the distance from the stagnation point increased, the Nusselt number decreased sharply [4]. Since the stagnation point of the direct jet didn^{\prime}t change with time, the effective cooling area was fixed, and the influence range of the flow field disturbance was limited. With the development of flow, the gradually thickened boundary layer would negatively affect heat transfer [5]. The fluidic oscillator was a unique device that could transform a steady-state jet into an oscillating jet. This oscillation was self-induced and self-sustained [6]. It could be considered as a jet generator that increased the disturbance range of the flow field due to its oscillation characteristics. The potential of fluidic oscillators for flow control had been the subject of many previous studies [7, 8]. Bobusch et al. [9] used particle image velocimetry and time-resolved pressure measurement in water to visualize and quantify the internal flow patterns inside the fluid oscillator. The external flow field properties of a fluidic oscillator were investigated by Gregory et al. [10]. They used the pressure-sensitive material to make unsteady time-resolved measurements of the jet oscillations and evaluated the dependence of frequency on velocity. Arwatz et al. [11] altered the geometry of a fluidic oscillator and studied the changes in flow characteristics such as the oscillation frequency. Metka et al. [12] studied drag reduction on the generic vehicle model that used a spanwise array of fluidic oscillators with quasi-steady blowing at the roof-slant interface. The performance of an airfoil equipped with a high-lift system was enhanced by the manipulation of vorticity concentrations near the airfoil surface using arrays of fluidic oscillators [13]. Besides, plasma-fluidic actuators [14], piezoelectric actuators [15], and fluidic diverters [16] were some other examples of such fluidic oscillators currently being studied for flow control.

Researchers did much work to explore the characteristic scales associated with the oscillation frequency and identify the mechanism that drives the jet oscillation [17]. Some studies optimized the geometric model and changed the characteristics of the external flow field to achieve the purpose of enhancing heat transfer [18]. Enhancement of impingement heat transfer using a self-oscillating jet impingement nozzle was described by Page et al.

* Corresponding author.
E-mail address: yjwu2019@whut.edu.cn (Y. Wu).

https://doi.org/10.1016/j.ijheatmasstransfer.2021.121515
0017-9310/

Nomenclature

Symbols

$C_{1\varepsilon}, C_{2\varepsilon}, C_\mu, \eta_0$	Empirical constants in the RNG $k-\varepsilon$ model
c_p	Thermal capacity $(J \cdot K^{-1} \cdot kg^{-1})$
D,D_f	Characteristic length (mm)
G_k	Turbulent kinetic energy caused by the velocity gradient $(m^2 \cdot s^{-2})$
P	Pressure (Pa)
Pr_T	Turbulent Prandtl number
Nu	Nusselt number
q'	Heat flux $(W \cdot m^{-2})$
u_{in}	Inlet velocity $(m \cdot s^{-1})$
k	Turbulence kinetic energy $(J \cdot kg^{-1})$
L	Length of the target surface in the X direction (mm)
Re	Reynolds number
S_{ij}	Deformation rate tensor
t	Time (s)
T	Temperature (K)
T_f	Oscillating period (s)
W	Length of the target surface in the Z direction (mm)
X, Y, Z	Cartesian coordinates
$\alpha_k, \alpha_\varepsilon$	Inverse effective Prandtl numbers for k and ε
$\sigma_{\omega,2}, \gamma_2, \beta_2, \sigma_k, \beta^*$	Factors in the $k-\omega$ SST model
ω	Turbulence frequency
τ_{ij}	Reynolds stresses $(kg \cdot m^{-1} \cdot s^{-1})$
ε	Turbulent dissipation rate
λ	Thermal conductivity $(W \cdot K^{-1} \cdot m^{-2})$
μ	Dynamic viscosity $(kg \cdot m^{-1} \cdot s^{-1})$
ρ	Density $(kg \cdot m^{-3})$

Abbreviations

RANS	Reynolds-averaged Navier-Stokes
ELES	Embedded large eddy simulation
SST	Shear stress transport
RNG	Renormalization Group
SIMPLE	Semi-implicit method for pressure linked equations

[19]. The self-oscillating jet distributed the pressure over the impingement surface area in a less concentrated manner than that of a standard jet impingement nozzle and demonstrated higher heat transfer close to a surface. Agricola et al. [20] measured the heat transfer coefficient of an impinging sweeping jet by experiment and compared it with a steady circular orifice jet. Hossain et al. [21]studied the external flow field and heat transfer performance for both steady and sweeping jets under three configurations with different curvature radiuses of the impingement surface. Lundgreen et al. [22] numerically studied the heat removal performance of the sweeping jet with different nozzle-plate spacing. When the nozzle-plate spacing was small, the average Nusselt number of the sweeping jet was higher than that of the direct jet. Thurman et al. [23] applied the sweeping jet to heat transfer and evaluated the effect of the jet ejected through a hole into a cross-flow on the film cooling process. They discovered that the sweeping jet made the cooling performance more uniform on the surface than a jet from a spiral hole. Camci and Herr [24] found that the coverage area of the impingement zone was significantly enhanced because of the inherent sweeping motion of the oscillating coolant jet. The instantaneous jet position (relative phase) between adjacent oscillators may determine whether there was mutual interference between oscillators [25]. Gokoglu et al. [26] experimentally and numerically studied the synchronization of a fluidic oscillator array. They stated that synchronized fluidic oscillators would be more efficient than asynchronous ones for flow control and turbine film cooling applications. It was convenient to fabricate these oscillators using 3-D printing. Hossain et al. [27] carried out both experiment and numerical simulations to study the cooling performance of five sweeping air jets. Increasing hole spacing could provide larger lateral coverage without additional coolant requirements.

The heat transfer performance and flow field of impinging jets were affected by many parameters like jet Re number, jet-to-plate distance, angle of impingement surface, the characteristics of impingement surface, turbulence intensity, etc. [28, 29]. The inclined jet had become a choice in optimizing heat removal performance. The fluid flow and heat transfer distribution to an obliquely impinging air jet was reported by Beltaos [30]. Goldstein et al. [31] found that as the angle between the jet and the impinging surface decreased, the jet's elongation on the impinging surface increased. The oscillating jet perpendicular to the impingement surface could only enhance heat transfer on the sweeping path below the outlet throat. The oblique swing jet was found randomly oscillating during its impingement on the surface, resulting in an unstable flow field downstream [32]. The diffusion hole of the oblique fluidic oscillator could be used to provide more uniform and higher values of film effectiveness. The existence of lateral angles improved jet spreading [23].

Studies on the combination of the microchannel and the oblique fluidic oscillator array in a single device had rarely been reported. In this paper, the heat removal capacity of the microchannel heat exchanger with two parallel fluidic oscillators was studied. The fluidic oscillators were tilted at an angle of 30° above the impinging surface to enlarge the influence range of the jets on the external flow field. Unsteady RANS turbulence models were employed to study the fluid dynamic and the heat removal performance of the sweeping jets under different output phases. The heat exchange, pressure drop, and oscillatory frequency of two typical oscillation modes (co-directional oscillation and reverse oscillation) were numerically evaluated. This study could be used to guide the design of heat exchangers with many fluidic oscillator arrays distributed throughout the target surface for the cooling of a large surface.

2. Computational method

2.1. Geometric model

The geometric model consisted of fluidic oscillator arrays and a fluid channel below as depicted in Fig. 1(a). Water was chosen as the working fluid because of its high heat removal performance. After the sweeping jet impinged on the surface for the enhanced convective heat transfer, it diffused downstream of the channel and took away more heat. The heat transfer performance of two fluidic oscillators distributed along the span of the target surface was studied to reduce the computing resources. As shown in Fig. 1(b), the model's size was adjusted from the computational model used in Ref. [4], and the fluidic oscillators were set above the channel at an angle of 30°. Because too sparse oscillator arrangement would lead to high local temperature, while too dense oscillator arrangement would consume too much energy, the Z-direction spacing was set as 7.5D (D=1.0 mm). The fluidic oscillator mainly consisted of a power nozzle, a central mixing chamber, two feedback channels, and an exit throat. The thickness of the fluidic oscillator was 0.5D, and the height of the fluid channel was D. The exit hole had a 4D trailing edge. The nozzle entrance of the oscillator was expanded forward and parallel to the impinging surface, which allowed the jets to interact with the mainstream. The minimum

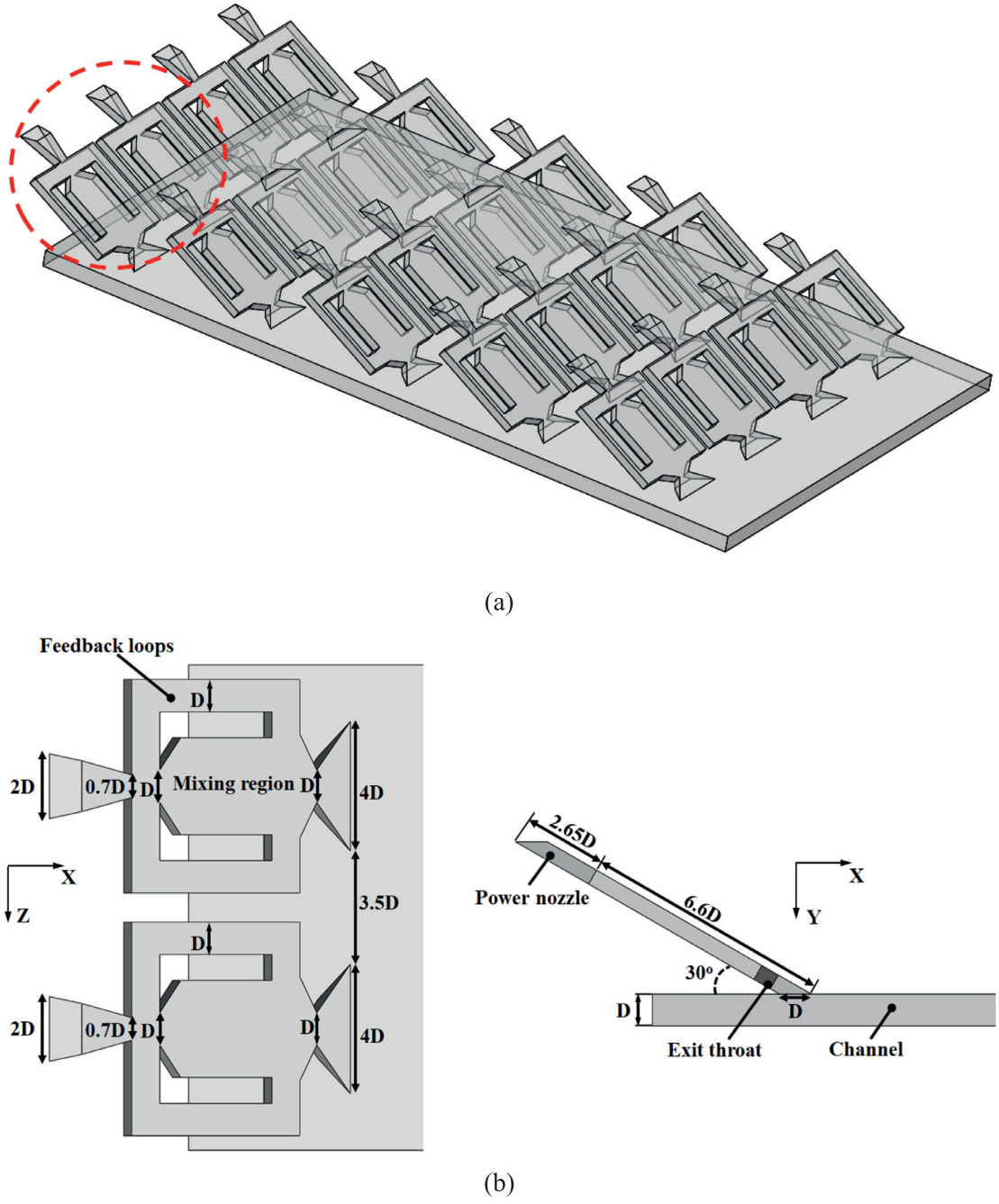

Fig. 1. (a) The oblique self-oscillating fluidic oscillator arrays; (b) The computational model.

width of the power nozzle was 0.7D. The outlet of the channel was 24D away from the center of the throat to make sure that the flow was fully developed and the outlet boundary condition would not significantly affect the fluid dynamics of the sweeping jets. A direct jet model was established for reference, whose sizes were consistent with the fluidic oscillator except no feedback channels.

2.2. Numerical model

2.2.1. The RNG $k-\varepsilon$ model

In this paper, the geometric model had a magnitude in millimeters, much larger than the free path of a molecular movement. The working medium flow satisfied the continuum hypothesis. The oscillatory frequencies and the heat removal performance predicted by the $k-\omega$ SST, a RANS turbulence model, matched well with the ELES model for all the cases in the work of Wu et al.[4]. The RANS turbulence model provided an economical way for modeling complex turbulent industrial flows. In this study, unsteady RANS simulations were conducted to study the fluid dynamic and heat transfer performance in the fluidic oscillator array. The RNG $k-\varepsilon$ model and the $k-\omega$ SST model were used to simulate the turbulence separately. The RNG $k-\varepsilon$ model incorporated an additional term in the turbulent energy dissipation equation based on strain rates and included adjustments for the viscous effects and the turbulent Prandtl number. This model was formulated for flows with high Reynolds numbers. It could model flows with a high strain rate and large streamline bending degree better [33]. The govern-

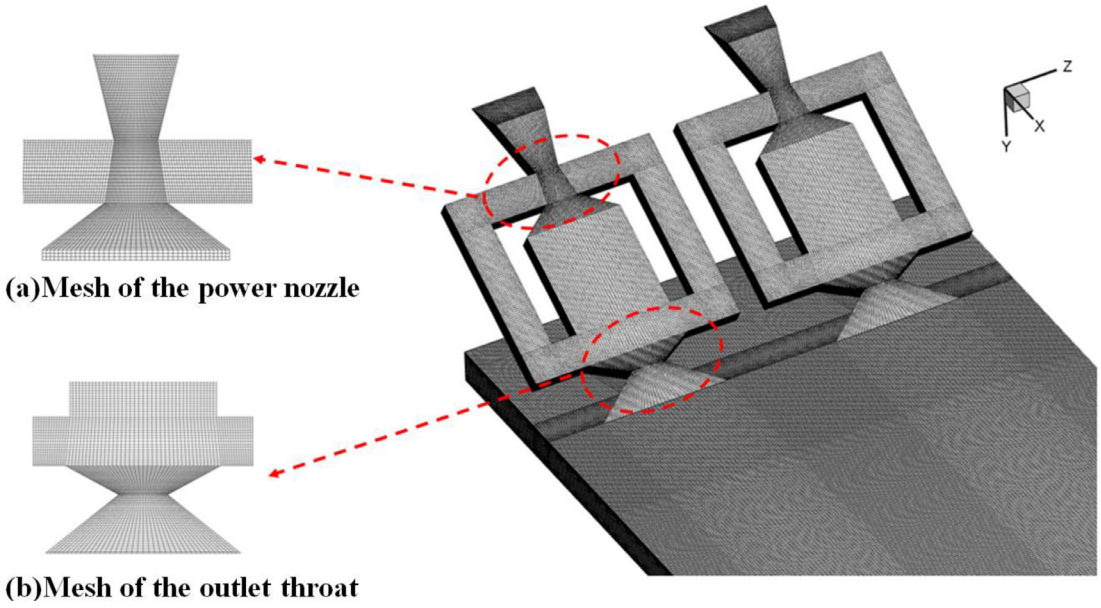

Fig. 2. Grid system of the computational model.

ing equations of incompressible flow in the microchannels were given as follows.

Continuity equation

$$\frac{\partial u_j}{\partial x_j} = 0 \tag{1}$$

Momentum equation

$$\frac{\partial(\rho u_i)}{\partial t} + \frac{\partial\left(\rho u_i u_j\right)}{\partial x_j} = -\frac{\partial p}{\partial x_i} + \frac{\partial}{\partial x_j}\left(\mu\frac{\partial u_i}{x_j} - \rho\overline{u'_i u'_j}\right) \tag{2}$$

Energy equation

$$\rho c_p\left[\frac{\partial T}{\partial t} + u_j\frac{\partial T}{\partial x_j}\right] = \frac{\partial\left(\lambda\frac{\partial T}{\partial x_j} - \rho c_p\overline{u'_j T'}\right)}{\partial x_j} \tag{3}$$

where $-\rho\overline{u'_i u'_j}$ and $-\rho c_p\overline{u'_j T'}$ were caused by turbulent pulsation. τ_{ij} represented thermal stress caused by viscosity which was calculated by $\tau_{ij} = -\rho\overline{u'_i u'_j} = 2\mu S_{ij}$. S_{ij} was the mean rate of strain tensor calculated by $S_{ij} = \frac{1}{2}(\frac{\partial\overline{u_i}}{\partial x_j} + \frac{\partial\overline{u_j}}{\partial x_i})$. k and ε represented the turbulent kinetic energy and turbulent dissipation rate, respectively.

Governing equation of k

$$\frac{\partial(\rho k)}{\partial t} + \frac{\partial(\rho k u_i)}{\partial x_i} = \frac{\partial}{\partial x_j}\left(\alpha_k\mu_{eff}\frac{\partial k}{\partial x_j}\right) + G_k + \rho\varepsilon \tag{4}$$

Governing equation of ε

$$\frac{\partial(\rho\varepsilon)}{\partial t} + \frac{\partial(\rho\varepsilon u_i)}{\partial x_i} = \frac{\partial}{\partial x_j}\left(\alpha_k\mu_{eff}\frac{\partial\varepsilon}{\partial x_j}\right) + \frac{C_{1\varepsilon}\varepsilon}{k}G_k - \left[C_{2\varepsilon} + \frac{\eta(1-\eta/\eta_0)}{1+\beta\eta^3}\right]\rho\frac{\varepsilon^2}{k} \tag{5}$$

where μ_{eff} represented the effective turbulent viscosity; Pr_T was turbulent Prandtl number. α_k and α_ε represented the inverse effective Prandtl numbers for k and ε, respectively, which could be set as 1.39 and 1.39, respectively. G_k denoted the generation of turbulent kinetic energy due to the average velocity gradient.η_0 was set as 4.38, β was volume coefficient of expansion could be set as 0.012, C_μ, $C_{1\varepsilon}$, and $C_{2\varepsilon}$ were empirical constants which could be set as 0.085, 1.42, and 1.68, respectively.

2.2.2. The $k-\omega$ SST model

The $k-\omega$ SST model could better predict the turbulent length scale than the $k-\varepsilon$ model. It could model the wall jet, both in the sublayer and logarithmic region, without the need for damping functions [33]. The model calculated the turbulent viscosity as a function of k and ω.

Governing equation of k

$$\frac{\partial(\rho k)}{\partial t} + \frac{\partial\left(\rho k u_j\right)}{\partial x_j} = \frac{\partial\left(\left(\mu+\frac{\mu_t}{\sigma_k}\right)\frac{\partial k}{\partial x_i}\right)}{\partial x_j} + \left(\tau_{ij}\cdot S_{ij} - \frac{2}{3}\rho k\frac{\partial u_i}{\partial x_j}\delta_{ij}\right) - \beta^*\rho k\omega \tag{6}$$

Governing equation of ω

$$\frac{\partial(\rho\omega)}{\partial t} + \frac{\partial\left(\rho\omega u_j\right)}{\partial x_j} = \frac{\partial\left(\left(\mu+\frac{\mu_t}{\sigma_{\omega,1}}\right)\frac{\partial\omega}{\partial x_i}\right)}{\partial x_j} + \gamma_2\left(2\rho S_{ij} - \frac{2}{3}\rho\omega\frac{\partial u_i}{\partial x_j}\delta_{ij}\right) - \beta_2\rho\omega^2 + 2\frac{\rho}{\sigma_{\omega,2}\omega}\frac{\partial k}{\partial x_k}\frac{\partial\omega}{\partial x_k} \tag{7}$$

where the σ_k, β^*, $\sigma_{\omega,2}$, γ_2 and β_2 were revised factors in $k-\omega$ model, with the corresponding values 2.0, 0.009, 1.17, 0.44, and 0.083, respectively. μ_t and $\sigma_{\omega,1}$ were related to the blending functions to make the equations suitable for both the near wall and far-field region [34].

2.3. Boundary conditions

In this simulation, the inlet was set at the entrance of the power nozzle. The inlet water had a uniform velocity and temperature of 300 *K*. The angle between the vector direction of inlet velocity and the inlet plane was 30 degrees. The relative outlet pressure was set to 0 *Pa*. The simulation was performed using water with the Reynolds number (Re) ranging from 3000 to 5000. The Reynolds number was defined as

$$\mathrm{Re} = \frac{\rho u_{in} D_f}{\mu} \tag{8}$$

where the inlet velocity u_{in} was estimated based on the throat hydraulic diameter D_f. A constant heat flux boundary condition, $q' = 10^6\ W/(m^2\cdot K)$, was set on the impinging wall. Other walls were assumed adiabatic and non-slip.

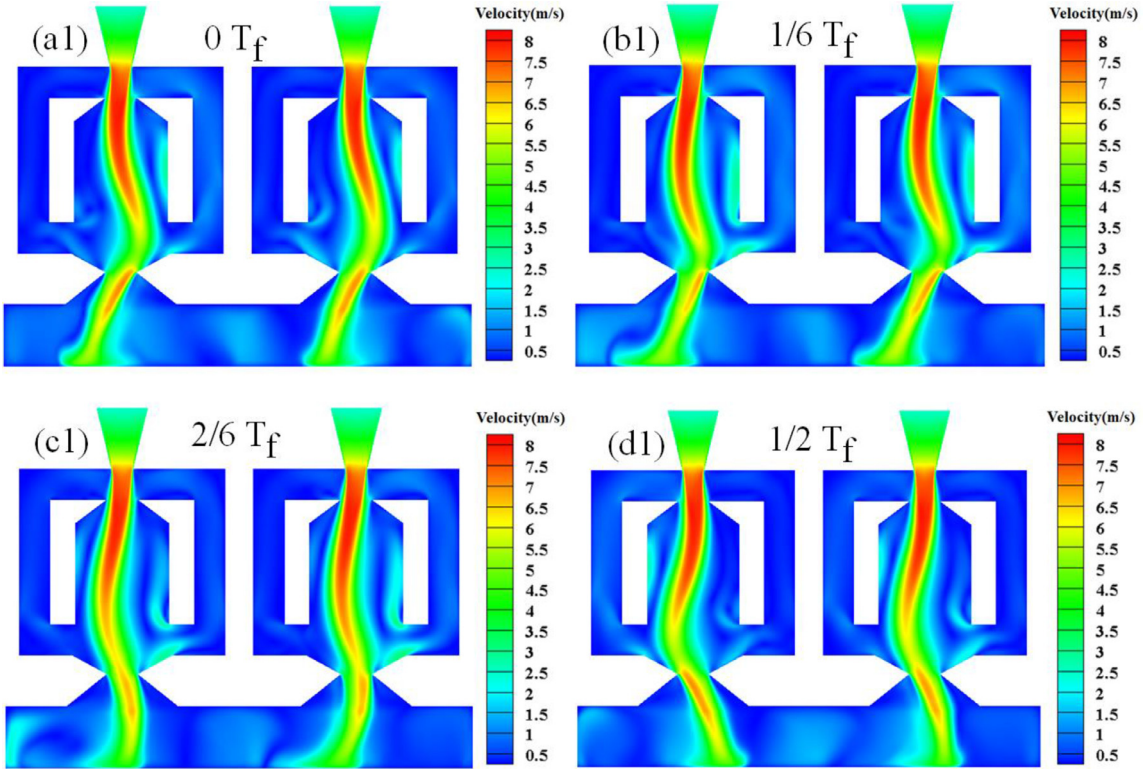

Fig. 3. (a1)-(d1)Time-resolved flow fields of co-directional oscillation for half of the sweeping period with Re = 5000.

2.4. Numerical methodology

In this simulation, ANSYS FLUENT19.0 was used for unsteady computation. The SIMPLE model was applied for pressure–velocity coupling. The Gauss-Green method was used for pressure discretization. The discretization method used for all the other parameters was the second-order upwind method to ensure numerical stability. A second-order implicit method was used in the time domain with a time step of 10^{-5} s to obtain time-resolved fluid dynamic and heat transfer results. The time step was estimated by the averaged velocity at the throat of the nozzle, where the flow mean velocity was high. The simulations were run until the oscillating was stable. The convergence residual for the energy equation was 10^{-7}, and that for other equations was 10^{-5}. The inlet turbulence intensities were set 3%, 4%, and 5% for Re = 3000, 4000, and 5000, respectively [35]. Steady-state RANS simulations were performed for all steady jet cases for reference.

The grid system was shown in Fig. 2. The computing domain adopted structured grid to save computational resources. The grids near the walls were densified to preserve a higher accuracy. A standard wall treatment was applied to near-wall modeling for the $k-\varepsilon$ model. The grid of the power nozzle and outlet throat of the fluidic oscillator was depicted in Fig. 2(a-b).

The grid independence was checked to validate the modeling results. Three grid systems with mesh numbers of 3,601,000, 4,219,000, and 5,060,000 were examined by the RNG $k-\varepsilon$ model. When Re = 5000, the oscillation frequencies were 122, 125, and 124, respectively. The simulation results were thought to be grid independent as the derivations of the oscillation frequency were less than 3% for all the simulation cases. The grid system with a grid number of 4,219,000 was chosen for numerical calculations. The grids near the walls were slightly modified to meet the requirement of the turbulence model. The dimensionless wall distance y^+ of the first node near the wall was set to around 10 for the RNG $k-\varepsilon$ model., while the grids near the canister wall were refined to y^+~1 for the transitional $k-\omega$ SST model. The grid system using for the direct jets was the same as the fluidic oscillators but with the two feedback channels removed. Thus the simulation results of the direct jets were assumed grid-independent.

3. Results and discussion

3.1. Fluid dynamic result

The fluidic oscillators worked based on bi-stable states of a jet of fluid in a cavity caused by a specially designed feedback path. The power jet coming out from the power nozzle would attach to one of the two side walls of the mixing chamber due to the Coanda effect [36]. Because of the asymmetric characteristics of the flow field, the pressure difference between the two feedback channels would cause a change in the direction of the jet. The jet within the mixing chamber executed an oscillatory motion, thus generated a sweeping jet through the outlet throat. In this simulation, a quasi-steady oscillating flow pattern was observed in each fluidic oscillator. Due to the random direction of the power jet from the nozzle at the initial time, the fluidic oscillators in the array had different oscillating modes. As the flow started to make its first pass through the fluidic oscillator, capturing the flow acceleration and the transient development of pressure and flow fields within the array accurately was crucial. We could observe the synchronous and asynchronous output phases. In this study, three typical fluid dynamic modes of co-directional oscillation, reverse oscillation, and irregular oscillation were analyzed.

Fig. 3-6 showed the time-resolved velocity fields and pressure fields of the array for half of the sweeping period with Re = 5000. From the velocity field in Fig. 3(a1)-(d1), we could observe the synchronous output phase. The duration of the oscillation period T_f could be calculated based on the oscillation frequency under different Re numbers in Fig. 10. At $0T_f$, the fluid jet was attached to the left side of the nozzle exit wall. The jet in the mixing chamber

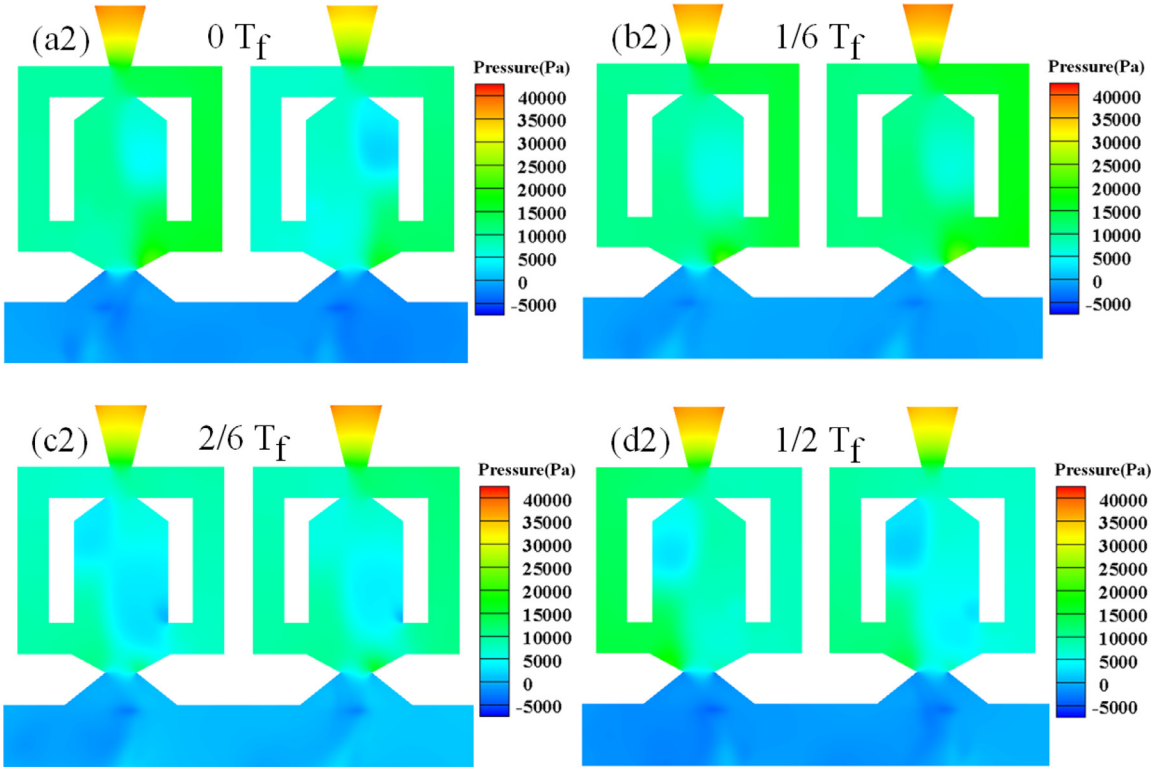

Fig. 4. (a2)-(d2) Time-resolved pressure fields of co-directional oscillation for half of the sweeping period with Re = 5000.

generated the flow through the upper feedback channel. At $1/6T_f$, the flow in the feedback channel interacted with the main jet in the inlet junction region. At $2/6T_f$, as the jet moved to the right side of the nozzle exit wall, the high-pressure region expanded into the left side of the mixing chamber and pushed the sweeping jet to the right side of the mixing chamber. As the flow in the feedback channel continued, the fluid jet was attached to the left side of the nozzle exit wall at $1/2T_f$. The fluidic oscillators in the array repeated the same process.

The velocity field in Fig. 5 depicted that the left and right fluidic oscillators were out of synch by a phase difference of 180 degrees. The flow fields inside the two oscillators were repeated periodically in a symmetrical flow pattern. When the fluid jets oscillated in the reverse direction, the pressure distribution of the two fluidic oscillators was approximately symmetric at each moment. Calculations showed that the design of the oscillators could generate the co-directional or reverse output according to the entrance boundary conditions of different Re numbers if the flow inside the array was initiated from quiescence. These two modes could be maintained stable in the unsteady simulation unless the inlet boundary conditions were actively changed. Moreover, if the flow field was initially asynchronous, resynchronization of the fluidic oscillators array was not practical since the flow was very sensitive to asymmetric perturbations and imperfections [26]. The reverse oscillation of the jets was a special case of the asynchronous output phase. As shown in Fig. 7, most outputs of the modes in the asynchronous phase were irregular. As shown in Fig. 8, the flow fields and pressure fields tended to be stable after removing the feedback channels.

Pressure drop was used to evaluate the resistance characteristics of different cases in this simulation, calculated by

$$\Delta P = P_{in} - P_{out} \tag{9}$$

where P_{in} was the average value of the relative static pressure at the left and right nozzle inlets over one full-time period. P_{out} was the relative static pressure of the channel outlet. Fig. 9 indicated the pressure drop for the sweeping jets and the direct jets. The pressure drop increased with the Re number in all the cases. The pressure drop predicted by the RNG $k-\varepsilon$ model is slightly higher than that of the $k-\omega$ SST model. Compared with the direct jet model, the fluidic oscillator contains feedback channels, which enhanced turbulence intensity. The pressure drop of the sweeping jets was higher than that of the direct jets under different Re numbers.

As depicted in Fig. 10, the oscillatory frequencies predicted by the RNG $k-\varepsilon$ model and $k-\omega$ SST model matched each other very well, with a difference of less than 3%. The oscillation frequency of the fluidic oscillator could be affected by many factors, such as the flow rate, feedback channel length, and working fluid. The fluidic oscillators had a linear flow versus frequency characteristic until it showed saturation that exceeded the corresponding flow rate [37]. It had been concluded in the open literature that the oscillation frequency of the fluidics was primarily a function of the volume flow rate within the investigated flow rate range [6]. As expected, the frequencies of the oscillatory jets almost linearly increased with the Re numbers.

3.2. Heat transfer result

Impinging jets helped fluid mix better and played a critical role in reducing boundary layer thickness, which could significantly improve heat transfer. Compared with the direct jet, the oscillating jet had a larger sweep range and a wider effective cooling coverage for the target surface [4]. Two typical modes, the co-directional oscillation and the reverse oscillation, were selected to analyze the heat transfer performance in this study.

Fig. 11 showed the time-resolved temperature contours of the fluidic oscillator array with Re=5000 using two different turbulence models. Fig.11(a1)-(b1) and (a2)-(b2) showed the temperature contours at $0T_f$ and $1/2T_f$ when the jets oscillated in the re-

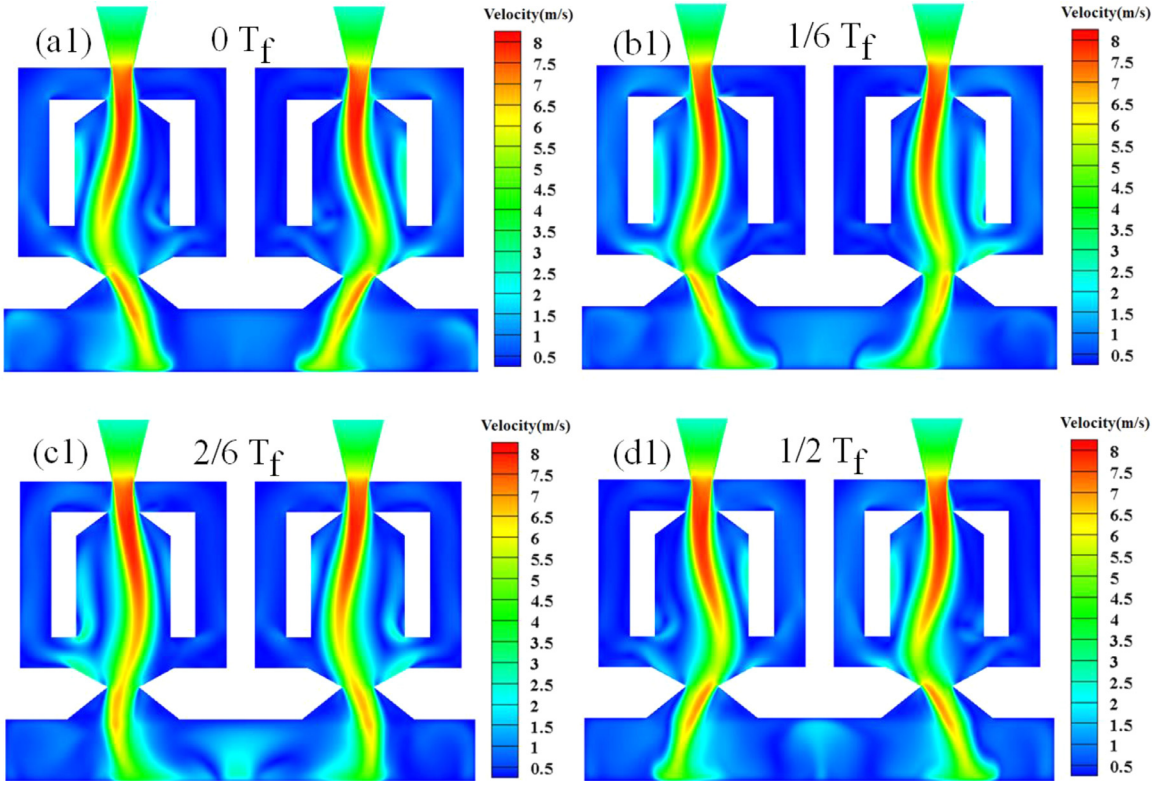

Fig. 5. (a1)-(d1)Time-resolved flow fields of the reverse oscillation for half of the sweeping period with Re = 5000.

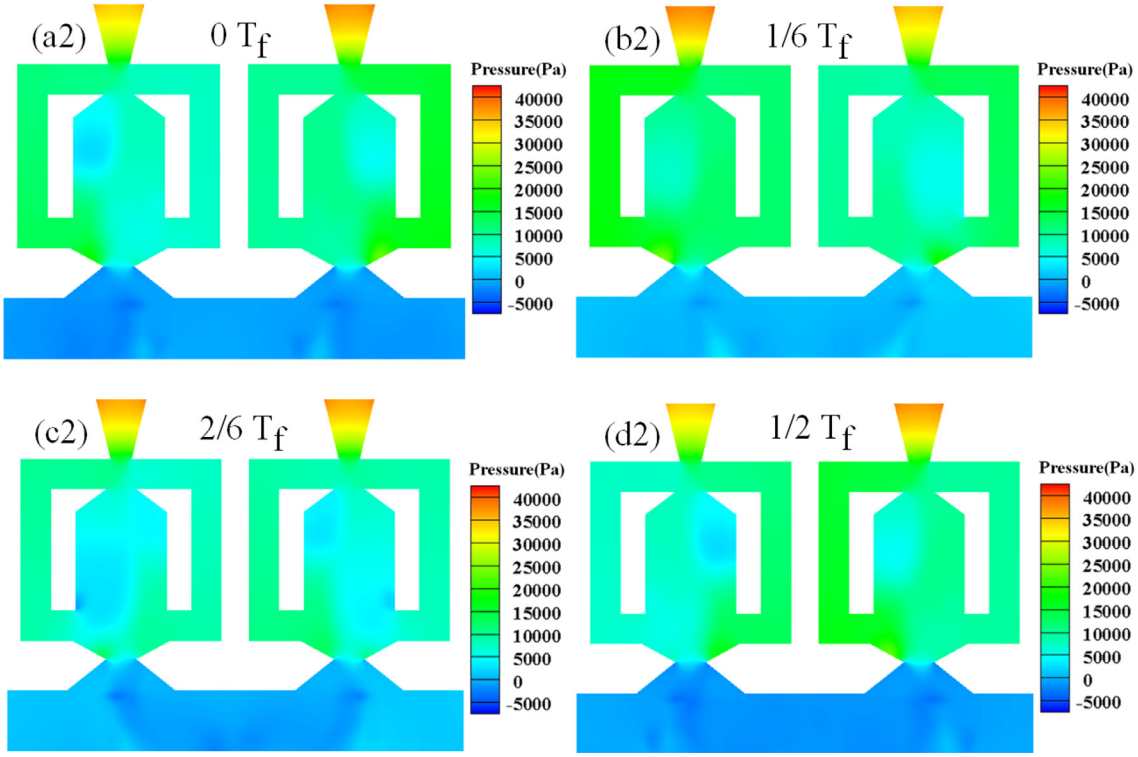

Fig. 6. (a2)-(d2) Time-resolved pressure fields of the reverse oscillation for half of the sweeping period with Re = 5000.

verse direction. Fig.11 (c1)-(d1) and (c2)-(d2) showed the temperature contours at $0T_f$ and $1/2T_f$ when the jets oscillated in the same direction. The oblique sweeping jets generated by the fluidic oscillators introduced strong turbulence near the impingement wall, which could help to enhance the convective heat transfer. Fig. 12 showed the temperature contours of the direct jets with Re=5000 using two different turbulence models. It was evident that the fluid temperature in the channel of the direct jet was higher than that of the oscillating jet.

The time-averaged Nusselt number (Nu) was used to evaluating the heat transfer performance of the jets. The Nusselt number was

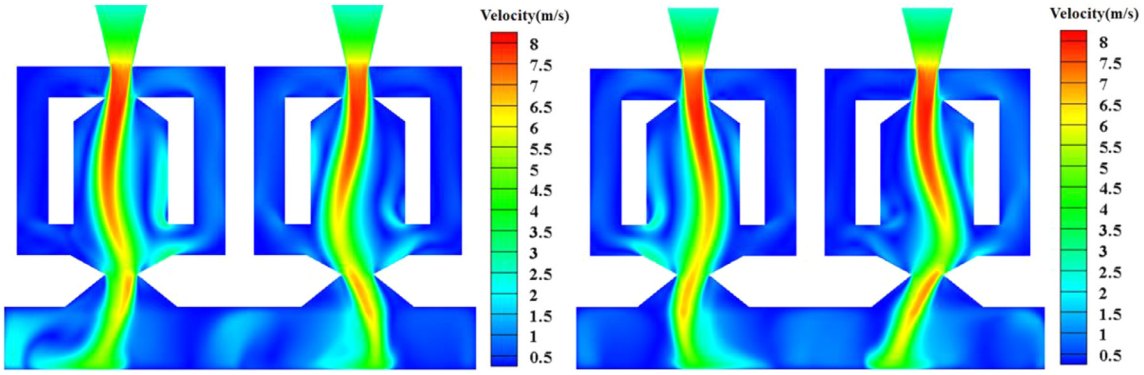

Fig. 7. Instantaneous flow fields of the irregular oscillation with Re = 5000.

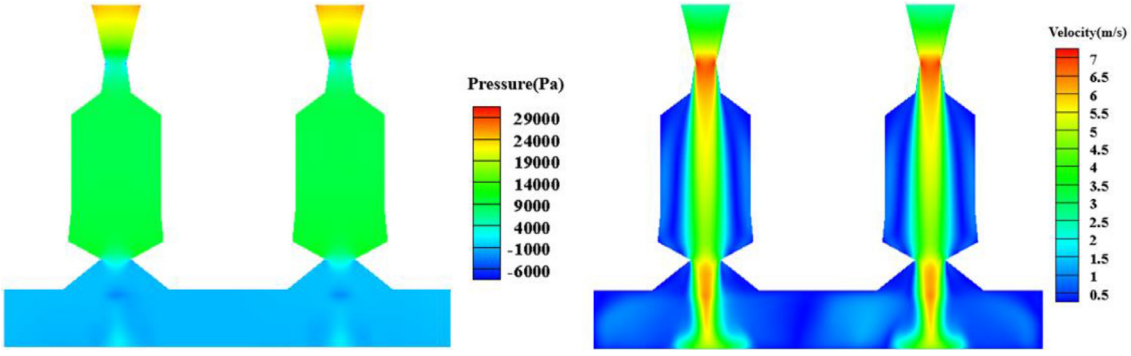

Fig. 8. Pressure fields and flow fields of the direct jets with Re = 5000.

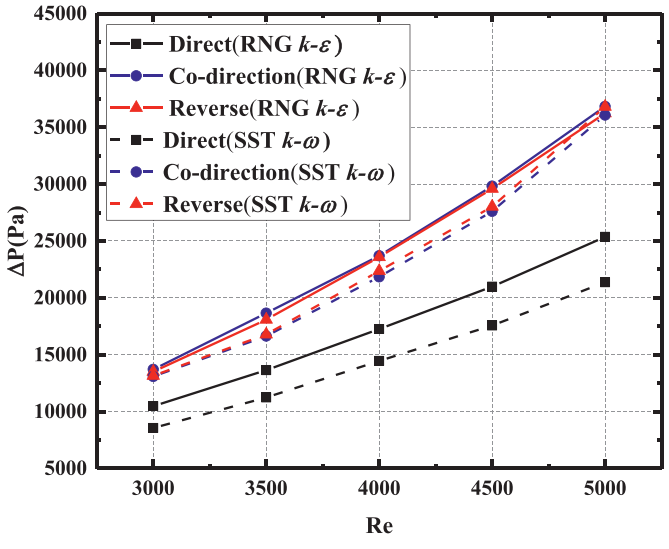

Fig. 9. The pressure drop of the jets under Re from 3000 to 5000

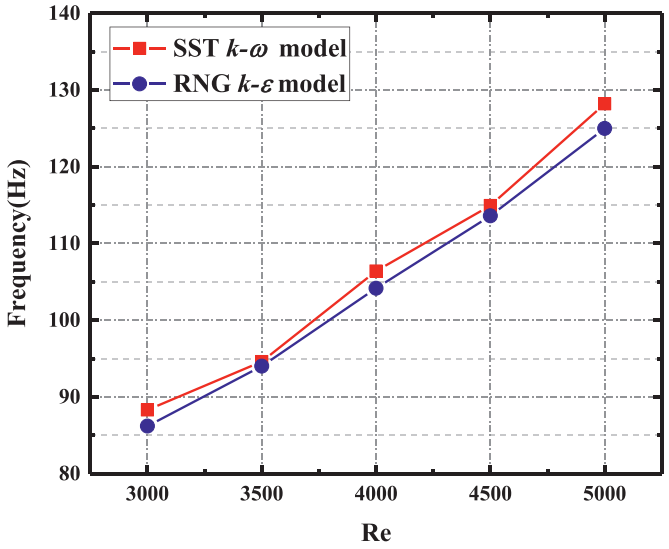

Fig. 10. The oscillatory frequency of the sweeping jet under Re from 3000 to 5000

defined as

$$Nu = \frac{q' D_f}{\lambda (T - T_i)} \tag{10}$$

where q' was the constant heat flux of the impingement surface, T and T_i were local surface temperature and jet inlet temperature, respectively. An area of $L \times W = 9 \times 15$ mm^2 on the impact surface was selected as the target area in this study. Fig. 13 showed the time-averaged Nu number contours on the target surface for the sweeping and direct jets at Re = 3000 and 5000. The data were averaged over one full-time period for each case. When the oblique direct jets impinged on the surface, the flow rapidly separated at the stagnation point and generously spread in the jet centerline stretching direction. Generally, the sweeping jets created a wider high-Nu-number zone than the direct jets. The oblique direct jets increased the elongation of the jet in the X direction on the target surface, but the Nu number dropped sharply from the stagnation point to both sides in the Z direction. However, when the sweeping jets oscillated in the same direction or in the reverse direction, the Nu number distribution in the direct impact area was more uniform. And the coverage area of the sweeping jets increased with Re number. The elongation range of the wall jet on the target sur-

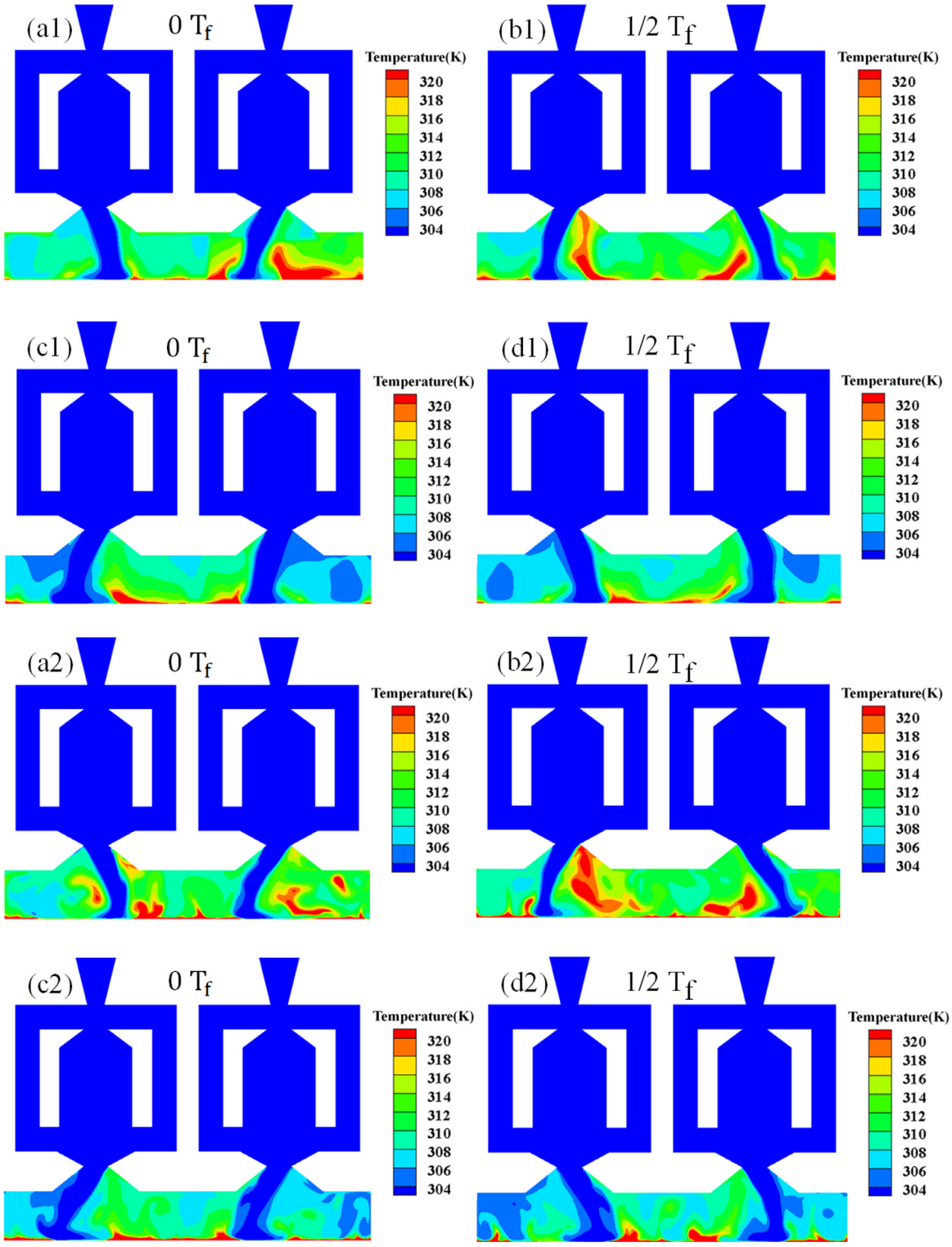

Fig. 11. Instantaneous temperature contours of the fluidic oscillators using RNG $k-\varepsilon$ model with Re = 5000: (a1)-(b1) reverse oscillation, (c1)-(d1) co-directional oscillation. Instantaneous temperature contours of the fluidic oscillators using $k-\omega$ SST model with Re = 5000: (a2)-(b2) reverse oscillation, (c2)-(d2) co-directional oscillation..

face provided the basis for the arrangement interval of the fluidic oscillators throughout the whole cooling surface.

Fig. 14 showed time-averaged Nu number distribution for the sweeping jets and the direct jets on the channel lines(X/L =0.25 and X/L=0.5) under Re from 3000 to 5000. The channel line X/L=0.25 represented the domain that was directly impacted by the jet. It could be seen that each curve had two peaks. Though the direct jets owned a relatively narrow high-Nu-number zone, the maximum Nu number of the direct jets was larger than the sweeping jets. As shown in Fig. 14(e), the Nu number reduced sharply from the center of impinging zone to both sides. The maximum heat transfer point almost coincided with the center

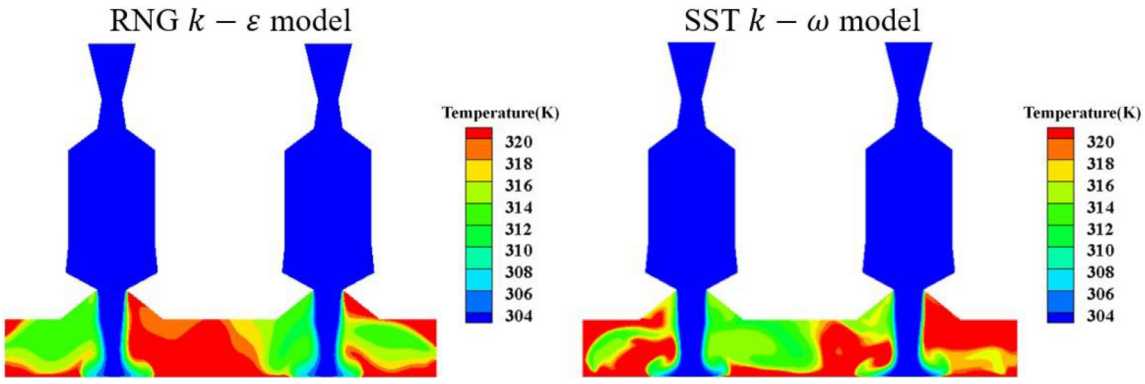

Fig. 12. Temperature contours of the direct jets with Re = 5000.

of the impact area. It could be seen from Fig. 14 (a) and (c) that increasing the Re number enhanced the diffusion effect but didn^{\prime}t strengthen the local extremum. This phenomenon happened because the oscillation frequency increased with the Re number. Thus, the sweeping jets^{\prime} duration on the stagnation point decreased. As a result, the total mass flow of the jet impinging on the heating surface per unit time didn^{\prime}t increase significantly at the stagnation point. Due to the interaction between turbulence and the vertical wall of the channel, the high-Nu-number region with a steep rise was observed in the position Z=0 m and Z=0.015 m. When the jets oscillated in the same direction, it showed a better average temperature in the middle area of the target surface than that when the jets oscillated in the reverse direction at Re=4000 and 5000. This phenomenon could be reasoned by the flow field mutual interference in the middle area when the jets at the exit oscillated face to face.

The channel line X/L=0.5 represented the domain that was not directly affected by the jets. After the oblique oscillating jets impinged on the surface, the amplitude of the oscillating jets decayed continuously with the propagation distance. The wall jet was generated in the near-wall region from the stagnation point to a certain downstream distance. In this domain, the intensity of fluid disturbance was less than that near the jet stagnation point, and the overall heat transfer efficiency was inferior. The high-Nu-number region of the sweeping jet had a larger coverage area than the direct jet. It could be seen from Fig. 14(b) and Fig. 14(d) that the sweeping jets exhibited better temperature uniformity.

Fig. 15 showed that the time-average Nu number of the target surface increased with Re number for different oscillation modes. The heat and mass transfer process in the near-wall region was hard to model due to the large velocity and temperature gradients. As reported in some literature [38-41], the Nu number predicted by the RNG $k-\varepsilon$ model and the $k-\omega$ SST model could be significantly different. Zuckerman et al. [33] explained that the RNG $k-\varepsilon$ model tended to predict larger jet-spreading rates. The RNG $k-\varepsilon$ model might fail to predict the occurrence of secondary peaks in Nu number for the impinging jet problem. By introducing the blending functions, the $k-\omega$ SST model combined the good near-wall behavior with the robustness of the $k-\varepsilon$ model in the far-field in a numerically stable way. It demonstrated superior performance for the prediction of convection heat transfer in complex turbulent flows. However, it was also reported by Park et al. [42] that the $k-\omega$ model tended to overpredict the Nu number near the impingement zone due to its sensitivity to far-field boundary conditions. The difference in predicting the time-averaged Nu of the target surface between the RNG $k-\varepsilon$ model and the $k-\omega$ SST model was acceptable. In order to verify the accuracy of the simulation results, some literature validated the heat transfer results by using four or five turbulence models [43, 44]. The heat transfer results of five different turbulence models at Re=3000 were shown in Table 1. The Nu numbers of co-directional mode, reverse mode, and direct jets predicted by these five mathematical models showed differences of 1.2–42.2%, 4.2–41.5%, and 3.4–43%, respectively. The experimental results for the fluidic oscillator array using water as the working fluid were absent in the open literature. A comprehensive experiment would help to calibrate the modeling results.

Table 1
Comparison of the time-averaged Nu number between the validated turbulence models at Re = 3000.

Turbulence models	Co-direction	Reverse	Direct
Standard $k-\varepsilon$	41.97	40.63	30.67
RNG $k-\varepsilon$	38.91	38.22	29.62
Realizable $k-\varepsilon$	39.39	36.59	22.12
Standard $k-\omega$	26.31	27.17	17.48
SST $k-\omega$	24.25	23.74	19.88

Compared with the direct jet, the average Nu number predicted by the RNG $k-\varepsilon$ model for the co-directional oscillation mode demonstrated an 8.7–31.4% increase, while the result predicted by the $k-\omega$ SST model represented a 4.8–19.4% increase. The average Nu number predicted by the RNG $k-\varepsilon$ model for the reverse oscillation mode demonstrated an 8.1–28.9% increase, while the result predicted by the $k-\omega$ SST model represented a 6.5–22.7% increase. Because the same output phase of the irregularly oscillating jets couldn't be controlled under different Re numbers, it was hard to compare the heat transfer results under a particular mode. The results of the time-averaged Nu number over the target surface under several irregular modes were shown in Fig. 15. Generally, the heat dissipation performance of the jets oscillating in different directions was better than that of direct jets. The growth rate of the time-averaged Nu number with Re of the sweeping jets was smaller than that of the direct jets.

The average Nu numbers of the co-directional and reverse oscillations predicted by the RNG k-ε model were approximated by empirical Eqs. (11) and (12), respectively.

$$Nu = 0.481Re^{0.551} \tag{11}$$

$$Nu = 0.379Re^{0.577} \tag{12}$$

The average Nu numbers of the co-directional and reverse oscillations predicted by the SST $k-\omega$ model were approximated by empirical Eqs. (13) and (14), respectively.

$$Nu = 0.314Re^{0.544} \tag{13}$$

$$Nu = 0.337Re^{0.532} \tag{14}$$

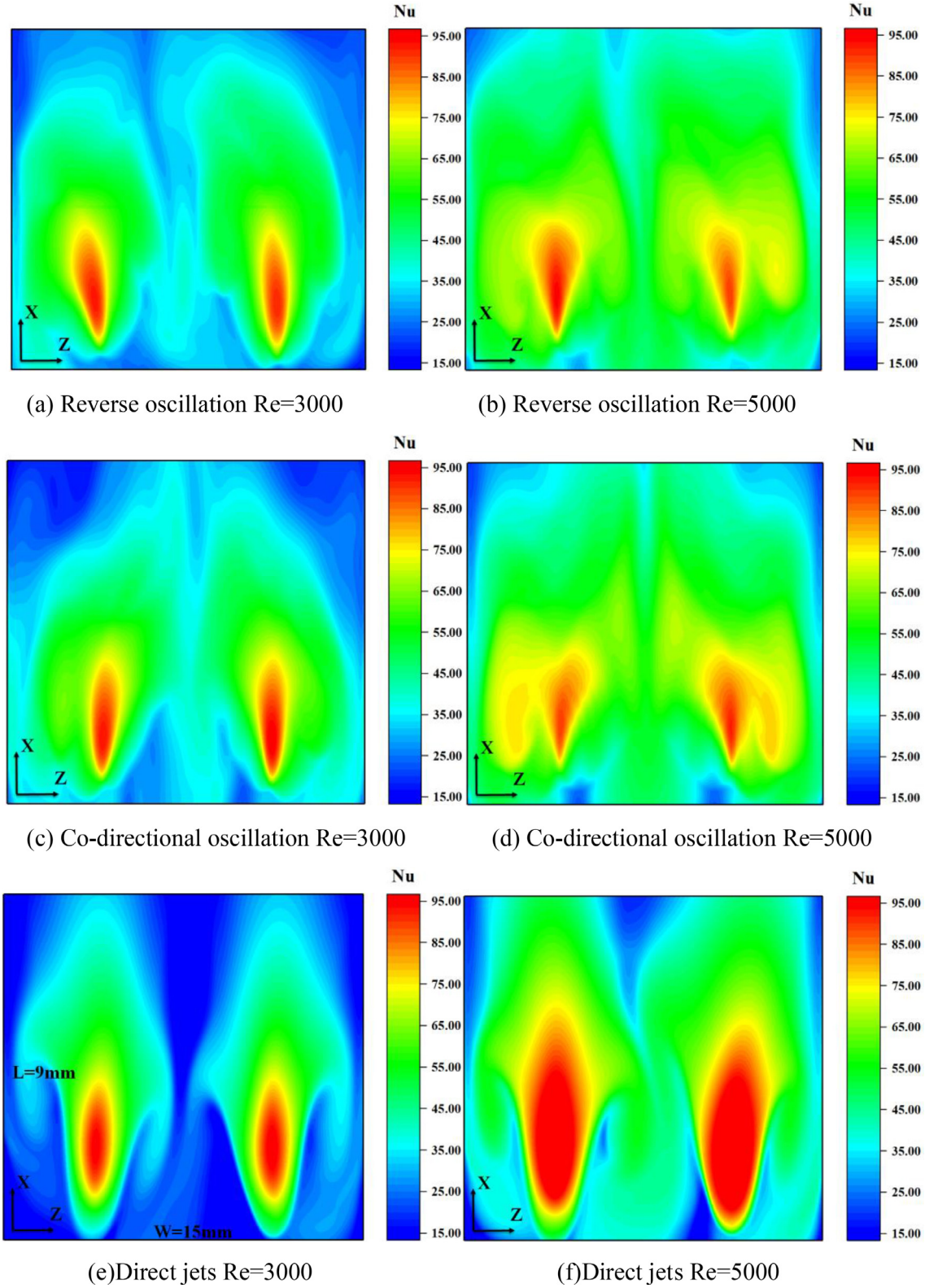

Fig. 13. Time-averaged surface Nu number contours on target surface for the sweeping jets and direct jets at Re = 3000 and 5000 using RNG $k-\varepsilon$ model.

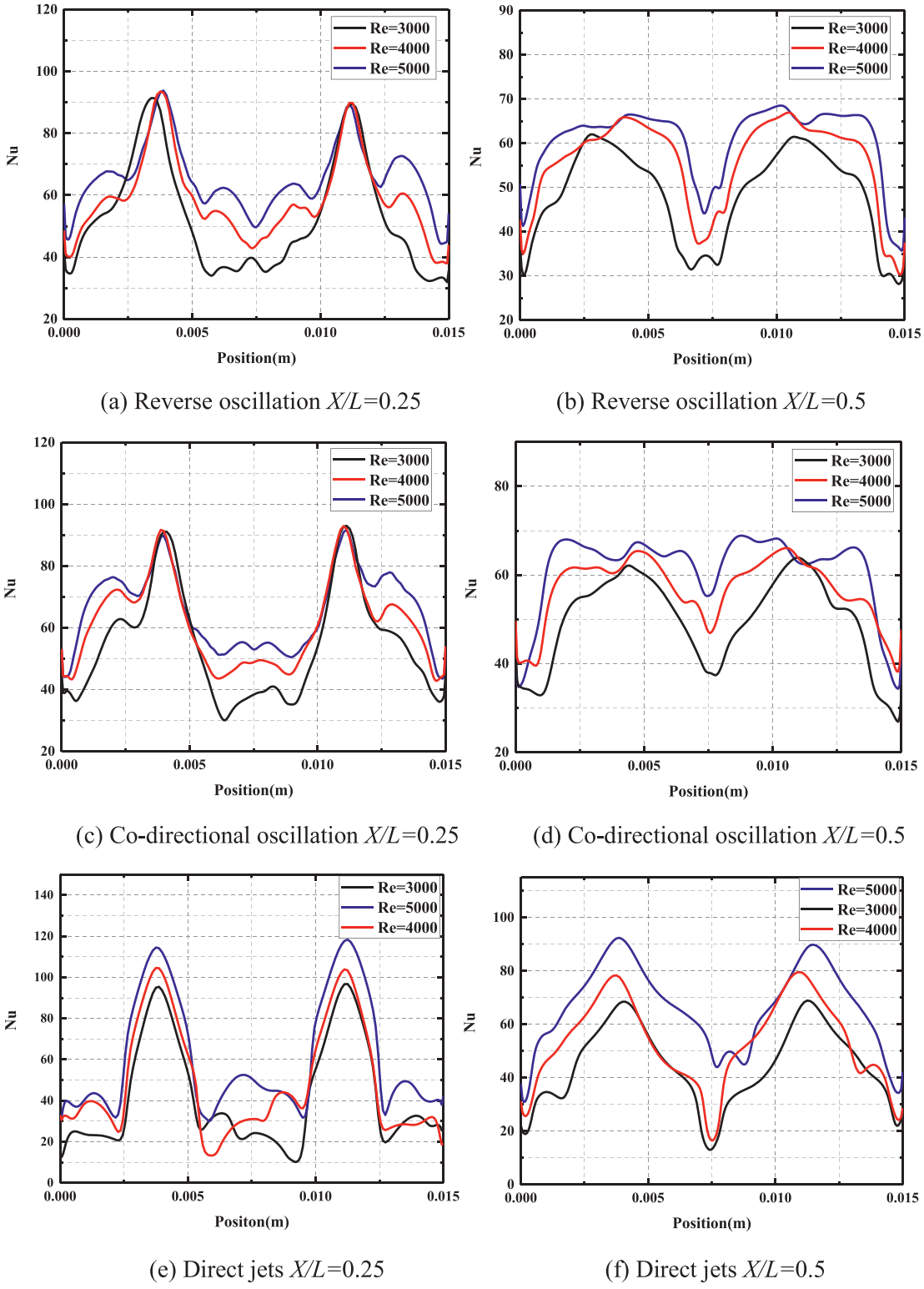

Fig. 14. Time averaged Nu number distribution for the sweeping jets and the direct jets on the channel lines(X/L=0.25 and X/L=0.5) under Re from 3000 to 5000.

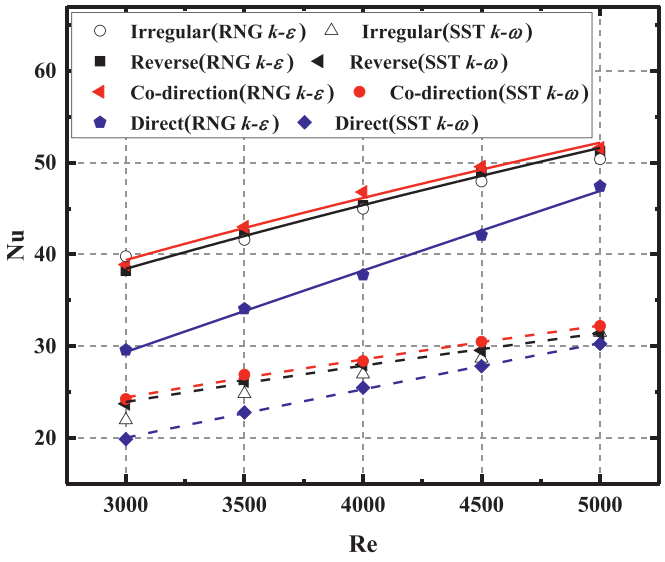

Fig. 15. Time-averaged Nu number over the target surface ($9 \times 15\ mm^2$)

The equations only worked for water, whose Pr number varied from 3.77 to 5.90 in the temperature range of 300-320 K. For other working fluids, the equations' coefficients should be adjusted accordingly.

4. Conclusions

Unsteady RANS simulations were conducted to study the fluid dynamic and heat transfer performance of the sweeping jets generated by an oblique fluidic oscillator array. The time-resolved pressure and flow fields were examined to understand the unsteady flow structure. The impact of Re and oscillation modes on heat transfer were discussed by studying the instantaneous temperature contours and the time-averaged Nu number on the target surface. According to the modeling results, the following conclusions could be drawn:

(1) Due to the oblique placement of the fluidic oscillator array, the elongation of the jet and the coverage of the impact area increased significantly. The flow characteristics of the fluidic oscillator array provided a basis for the design of the next-generation high-performance heat exchangers.

(2) Both the $k-\omega$ SST model and the RNG $k-\varepsilon$ model were used to conduct the turbulence simulations. The oscillatory frequencies predicted by the two models matched each other very well for different Re numbers. The pressure changes inside the fluidic oscillator drove the jet to deflect and formed a sweeping jet at the outlet. By studying the time-resolved pressure and flow fields, it was observed that the parallel oscillators had three oscillation modes, including co-directional oscillation, reverse oscillation, and irregular oscillation. The pressure loss of the sweeping jet increased with the Re number and was higher than that of the direct jet.

(3) The averaged heat transfer performance of the jets for the co-directional and reverse oscillations increased with Re numbers. The sweeping jets showed better temperature uniformity in the zone directly affected by the jet and the zone downstream. With Re varying from 3000 to 5000, the co-directional oscillation mode demonstrated 8.7–31.4% and 4.8–19.4% increase in the Nu number using the $k-\varepsilon$ model and the $k-\omega$ model, respectively. The Nu number for reverse oscillation increased by 8.1–28.9% and 6.5–22.7%, respectively, using the two turbulence models. The trend of time-average Nu number predicted by RNG $k-\varepsilon$ model and $k-\omega$ SST model was consistent. However, the exact values predicted by the two turbulence models showed a difference of 30-40%. The heat removal performance of the sweeping jets was almost equivalent under different oscillation modes.

The sweeping jets generated by the fluidic oscillator array created higher averaged Nu numbers and more uniform temperature on the target surface than the direct jets. Micro-channel heat exchangers integrated with the fluidic oscillator arrays were promising for the cooling of electronics with large surfaces. Experimental investigations and higher fidelity simulations would be performed for such kind of microchannel in the future.

Declaration of competing interest

The authors whose names are listed immediately below certify that they have **NO** affiliations with or involvement in any organization or entity with any financial interest (such as honoraria; educational grants; participation in speakers' bureaus; membership, employment, consultancies, stock ownership, or other equity interest; and expert testimony or patent-licensing arrangements), or non-financial interest (such as personal or professional relationships, affiliations, knowledge or beliefs) in the subject matter or materials discussed in this manuscript.

Acknowledgments

This research was supported by the European Commission H2020 Marie Curie Research and Innovation Staff Exchange (RISE) award (Grant No. 871998), the National Key Research and Development Plan (Key Special Project of Inter-governmental National Scientific and Technological Innovation Cooperation, Grant No. 2019YFE0197500), Key Research and Development Projects of Hubei Province (Grant No. 2020BAB129), Key Project of ESI Discipline Development of Wuhan University of Technology (Grant No. 2017001), and the Scientific Research Foundation of Wuhan University of Technology (Grant Nos. 40120237 and 40120551).

References

[1] T. Gan, T. Ming, W. Fang, Y. Liu, L. Miao, K. Ren, M.H. Ahmadi, Heat transfer enhancement of a microchannel heat sink with the combination of impinging jets, dimples, and side outlets, J. Thermal Anal. Calorimetr. (2019) 1–12.
[2] A. Dewan, P. Srivastava, A review of heat transfer enhancement through flow disruption in a microchannel, J. Therm. Sci. (2015).
[3] J.H. Lienhard, Liquid jet impingement, Ann. Rev. Heat Transfer 6 (6) (1995) 199–270.
[4] Y. Wu, S. Yu, L. Zuo, Large eddy simulation analysis of the heat transfer enhancement using self-oscillating fluidic oscillators, Int. J. Heat Mass Transf. 131 (MAR) (2019) 463–471.
[5] T. Ming, C. Peng, J. Gui, Y. Tao, Analysis on the hydraulic and thermal performances of a microchannel heat sink with extended-nozzle impinging jets, Heat Transf. Res. 48 (10) (2016).
[6] F. Ostermann, R. Woszidlo, C. Nayeri, C.O. Paschereit, Experimental comparison between the flow field of two common fluidic oscillator designs, Aiaa Aerospace Science Meeting, 2015.
[7] C. Cerretelli, K. Kirtley, Boundary layer separation control with fluidic oscillators, J. Turbomach. 131 (4) (2009) 29–38.
[8] R. Woszidlo, T. Stumper, C.N. Nayeri, C.O. Paschereit, Experimental study on bluff body drag reduction with fluidic oscillators, 52nd Aerospace Science Meeting, 2014.
[9] B.C. Bobusch, R. Woszidlo, J. Bergada, C.N. Nayeri, C.O. Paschereit, Experimental study of the internal flow structures inside a fluidic oscillator, Exp. Fluids 54 (6) (2013) 1559.
[10] J. Gregory, J. Sullivan, G. Raman, S. Raghu, Characterization of a micro fluidic oscillator for flow control, in: 2nd AIAA Flow Control Conference, 2004, p. 2692.
[11] G. Arwatz, I. Fono, A. Seifert, Suction and oscillatory blowing actuator modeling and validation, AIAA J. 46 (5) (2008) 1107–1117.
[12] M. Metka, J.W. Gregory, Drag reduction on the 25-deg ahmed model using fluidic oscillators, J. Fluid. Eng. 137 (5) (2015).
[13] M. DeSalvo, E. Whalen, A. Glezer, High-lift enhancement using fluidic actuation, in: 48th AIAA Aerospace Sciences Meeting Including the New Horizons Forum and Aerospace Exposition, 2010, p. 863.

[14] J. Gregory, J. Ruotolo, A. Byerley, T. McLaughlin, Switching behavior of a plasma-fluidic actuator, in: 45th AIAA Aerospace Sciences Meeting and Exhibit, 2007, p. 785.
[15] J.W. Gregory, E.P. Gnanamanickam, J.P. Sullivan, S. Raghu, Variable-frequency fluidic oscillator driven by a piezoelectric bender, AIAA J. 47 (11) (2009) 2717–2725.
[16] D. Culley, Variable frequency diverter actuation for flow control, in: 3rd AIAA Flow Control Conference, 2006, p. 3034.
[17] J.H. Seo, R. Mittal, Computational modeling and analysis of sweeping jet fluidic oscillators, in: 47th AIAA Fluid Dynamics Conference, 2017, p. 3312.
[18] D.J. Kim, S. Jeong, T. Park, D. Kim, Impinging sweeping jet and convective heat transfer on curved surfaces, Int. J. Heat Fluid Flow 79 (2019) 108458.
[19] R. Page, P. Chinnock, J. Seyed-Yagoobi, Self-oscillation enhancement of impingement jet heat transfer, J. Thermophys. Heat Transfer 10 (2) (1996) 380–382.
[20] L. Agricola, R. Prenter, R. Lundgreen, M. Hossain, A. Ameri, J. Gregory, J. Bons, Impinging sweeping jet heat transfer, in: 53rd AIAA/SAE/ASEE Joint Propulsion Conference, 2017, p. 4974.
[21] M.A. Hossain, L. Agricola, A. Ameri, J.W. Gregory, J.P. Bons, Effects of curvature on the performance of sweeping jet impingement heat transfer, in: 2018 AIAA Aerospace Sciences Meeting, 2018, p. 0243.
[22] R.K. Lundgreen, M.A. Hossain, R. Prenter, J.P. Bons, J.W. Gregory, A. Ameri, Impingement heat transfer characteric of a sweeping jet, in: 55th AIAA Aerospace Sciences Meeting, 2017, p. 1535.
[23] D. Thurman, P. Poinsatte, A. Ameri, D. Culley, S. Raghu, V. Shyam, Investigation of spiral and sweeping holes, J. Turbomach. 138 (9) (2016).
[24] C. Camci, F. Herr, Forced convection heat transfer enhancement using a self-oscillating impinging planar jet, J. Heat Transfer 124 (4) (2002) 770–782.
[25] M.N. Tomac, J.W. Gregory, Phase-synchronized fluidic oscillator pair, AIAA J 57 (2) (2019) 670–681.
[26] S. Gokoglu, M. Kuczmarski, D. Culley, S. Raghu, Numerical studies of an array of fluidic diverter actuators for flow control, in: 41st AIAA Fluid Dynamics Conference and Exhibit, 2011, p. 3100.
[27] M.A. Hossain, R. Prenter, R.K. Lundgreen, A. Ameri, J.W. Gregory, J.P. Bons, Experimental and numerical investigation of sweeping jet film cooling, J. Turbomach. 140 (3) (2018).
[28] T.S. O'donovan, D.B. Murray, Fluctuating fluid flow and heat transfer of an obliquely impinging air jet, Int. J. Heat Mass Transf. 51 (25-26) (2008) 6169–6179.
[29] M. Kilic, T. Calisir, S. Baskaya, Experimental and numerical investigation of vortex promoter effects on heat transfer from heated electronic components in a rectangular channel with an impinging jet, Heat Transf. Res. 48 (5) (2017).
[30] S. Beltaos, Oblique impingement of circular turbulent jets, J. Hydraulic Res. 14 (1) (1976) 17–36.
[31] R. Goldstein, M. Franchett, Heat transfer from a flat surface to an oblique impinging jet, J. Heat Transfer 110 (1) (1988) 84–90.
[32] P. Zhao, M. Zhang, G. Yu, Flume experiments on the oscillating wall jet induced by the swing oblique impingement jet, Journal of Physics: Conference Series, IOP Publishing, 2019.
[33] N. Zuckerman, N. Lior, Jet impingement heat transfer: physics, correlations, and numerical modeling, Adv. Heat Transfer 39 (2006) 565–631.
[34] A.F.U.s. GuideAnsys Fluent Theory Guide, ANSYS Inc., 2013 November.
[35] W. Tao, Numerical heat transfer, in, Xi'an Jiaotong University Press, Xi'an, 2001.
[36] J. Gregory, M.N. Tomac, A review of fluidic oscillator development and application for flow control, in: 43rd AIAA Fluid Dynamics Conference, 2013, p. 2474.
[37] D. Guyot, B. Bobusch, C.O. Paschereit, S. Raghu, Active combustion control using a fluidic oscillator for asymmetric fuel flow modulation, in: 44th AIAA/ASME/SAE/ASEE Joint Propulsion Conference & Exhibit, 2008, p. 4956.
[38] H. Xiao, Z. Liu, W. Liu, Turbulent heat transfer enhancement in the mini-channel by enhancing the original flow pattern with v-ribs, Int. J. Heat Mass Transf. 163 (2020) 120378.
[39] K. Zhu, P. Yu, N. Yuan, J. Ding, Transient heat transfer characteristics of array–jet impingement on high-temperature flat plate at low jet-to-plate distances, Int. J. Heat Mass Transf. 127 (2018) 413–425.
[40] B. Lu, P.-X. Jiang, Experimental and numerical investigation of convection heat transfer in a rectangular channel with angled ribs, Exp. Therm. Fluid Sci. 30 (6) (2006) 513–521.
[41] S. Eiamsa-ard, P. Promvonge, Numerical study on heat transfer of turbulent channel flow over periodic grooves, Int. Commun. Heat Mass Transf. 35 (7) (2008) 844–852.
[42] T. Park, H. Choi, J. Yoo, S. Kim, Streamline upwind numerical simulation of two-dimensional confined impinging slot jets, Int. J. Heat Mass Transf. 46 (2) (2003) 251–262.
[43] A. Fasquelle, J. Pellé, S. Harmand, I.V. Shevchuk, Numerical study of convective heat transfer enhancement in a pipe rotating around a parallel axis, J. Heat Transf. 136 (5) (2014).
[44] W. Siddique, L. El-Gabry, I.V. Shevchuk, T.H. Fransson, Validation and analysis of numerical results for a two-pass trapezoidal channel with different cooling configurations of trailing edge, J. Turbomach. 135 (1) (2013).